Hydrogen-assisted Post-growth Doping of Tellurium into Molybdenum Disulfide Monolayers with Tunable Compositions

Yin, G.; Zhu, D.; Lv, D.; Zhang, Z.; Hashemi, A.; Krasheninnikov, A. V.; Komsa, H.-P.; Jin, C.;

Originally published:

February 2018

Nanotechnology 29(2018), 145603

DOI: https://doi.org/10.1088/1361-6528/aaabe8

Hydrogen-assisted Post-growth Substitution of Tellurium into Molybdenum Disulfide Monolayers with Tunable Compositions

To cite this article before publication: Guoli Yin *et al* 2018 *Nanotechnology* in press https://doi.org/10.1088/1361-6528/aaabe8

Hydrogen-assisted Post-growth Substitution of Tellurium into Molybdenum Disulfide Monolayers with Tunable Compositions

Guoli Yin[1, 5], *Dancheng Zhu*[1, 5]*Danhui Lv*[1], *Arsalan Hashemi*[2], *Zhen Fei*[1], *Fang Lin*[3], *Arkady V. Krasheninnikov*[2, 4], *Ze Zhang*[1], *Hannu-Pekka Komsa*[2, *], *and Chuanhong Jin*[1, *]

[1]State Key Laboratory of Silicon Materials, School of Materials Science and Engineering, Zhejiang University, Hangzhou, Zhejiang 310027, China

[2]COMP, Department of Applied Physics, Aalto University, P.O. Box 11100, 00076 Aalto, Finland

[3]College of Electronic Engineering, South China Agricultural University, Guangzhou 510642, China

[4]Institute of Ion Beam Physics and Materials Research, Helmholtz-Zentrum Dresden-Rossendorf, 01314 Dresden, Germany

[*]E-mail: hannu-pekka.komsa@aalto.fi and E-mail: chhjin@zju.edu.cn

[5]Athours contributed equally to this work

Abstract

Herein we report the successful doping of tellurium (Te) into molybdenum disulfide (MoS_2) monolayers to form $MoS_{2x}Te_{2(1-x)}$ alloy with variable compositions via a hydrogen-assisted post-growth chemical vapor deposition (CVD) process. It is confirmed that H_2 plays an indispensable role in the Te substitution into as-grown MoS_2 monolayers. Atomic-resolution transmission electron microscopy (TEM) allows us to determine the lattice sites and the concentration of introduced Te atoms. At a relatively low concentration, tellurium is only substituted in the sulfur sublattice to form

monolayer $MoS_{2(1-x)}Te_{2x}$ alloy, while with increasing Te concentration (up to ~27.6% achieved in this study), local regions with enriched tellurium, large structural distortions, and obvious sulfur deficiency are observed. Statistical analysis of the Te distribution indicates the random substitution. Density functional theory calculations are used to investigate the stability of the alloy structures and their electronic properties. Comparison with experimental results indicate that the samples are unstrained and the Te atoms are predominantly substituted in the top S sublattice. Importantly, such ultimately thin Janus structure of $MoS_{2(1-x)}Te_{2x}$ exhibits properties that are distinct from their constituents. We believe our results will inspire further exploration of the versatile properties of asymmetric 2D TMD alloys.

1. Introduction

Monolayer molybdenum disulfide, a representative member of the transition metal dichalcogenide (TMD) materials family, holds promise for applications in nanoelectronics and nanophotonics, along with the existing industrial applications of its bulk counterpart as a catalyst in hydrodesulphurization. The material properties of pristine 2D TMDs, as desired for certain applications, can be further tuned e.g. by controlling the type and content of dopants or by various chemical and physical functionalization approaches [1-5]. Among them, isoelectronic doping with homo-group element, that is, substitution between transition metal, i.e., molybdenum and tungsten, or chalcogen, i.e., sulfur, selenium and tellurium, to form the alloyed TMD monolayers, has drawn broad interest, as they could provide a tunable band gap over wide range of energies and with spatial composition modulation. Remarkable progress

has been made in the controlled growth of 2D TMD alloys and their device applications. For instance, Gong et al. reported[6] that optical band gap modulations of monolayer $MoS_{2(1-x)}Se_{2x}$ can be tuned between ~1.85 eV (in monolayer MoS_2) and ~1.54 eV (in monolayer $MoSe_2$) depending on the concentration of Se. Duan et al.[7] and Li et al.[8] demonstrated a carrier type modulation in $WS_{2(1-x)}Se_{2x}$ and $Mo_{1-x}W_xSe_2$ nanosheets, via either the substitution of S with Se or Mo with W. So far, previous reports [6-15] have mainly focused on the S- and Se-based systems including $Mo_xW_{1-x}S_2$, $Mo_xW_{1-x}Se_2$, $MoS_{2(1-x)}Se_{2x}$ and $WS_{2(1-x)}Se_{2x}$ etc, while alloys with Te have remained less studied.

$MoTe_2$ itself hosts several features that are distinct from other 2D TMDs: (i) The semiconducting 2H-phase $MoTe_2$ monolayer has the lowest energy band gap (~1 eV) among 2D Mo-dichalcogenides, and thus in principle it can provide a larger range of band gap tunability via alloying with tellurium. (ii) Strong spin-orbit coupling is expected in Te-based 2D TMDs associated with the heavy Te atom, which is relevant in spin- and valleytronics devices. (iii) The energy difference between semiconducting 2H phase and (semi-)metallic 1T' phase of 2D $MoTe_2$ is very small, <0.1 eV per unit cell, that may favor applications in data storage and in electronics via phase engineering [16-29]. (iv) Finally, the so-called type-II Weyl semimetal behavior in octahedral bulk $MoTe_2$ (also known as T_d phase) has been confirmed [30- 33]. Given the versatile structural and electronic properties of 2D $MoTe_2$, it is increasingly important to also investigate the Te-substituted Mo- and W-dichalcogenides.

So far, a number of methods have been proposed to prepare monolayer TMD alloys including the growth of single crystals by chemical vapor transport followed by

mechanical exfoliation (ME) [9-11], physical vapor deposition (PVD)[7, 12, 13], and one-step chemical vapor deposition (CVD)[6, 14, 15]. Of these, CVD is perhaps the most widely adopted method owing to its capability to prepare high-quality 2D TMD alloys with large flake sizes and with well-controlled morphology. Compared to S and Se, Te has relatively low chemical reactivity, and it still remains an open question whether it is feasible to substitute Te into as-formed 2D TMDs like MoS_2 via CVD. In this work, we describe our efforts on preparing $MoS_{2(1-x)}Te_{2y}$ ($y<=x$) monolayers via Te substitution into as-grown MoS_2 monolayer through a two-step post-growth CVD process. Raman spectra, PL and atomic-resolution ADF-STEM techniques were used to determine the lattice sites and concentration of substituted Te atoms. Our results confirm, that: (i) Hydrogen carrier gas plays an indispensable role in the substitution process. (ii) The composition of Te can be modulated by varying the reaction time and temperature during doping. (iii) The atomic structures of the final MoSTe monolayers depend on the Te concentration. In particular, the heavy structural distortions observed in higher concentrations, indicated that there exists an upper limit for the composition of the substituted Te atoms through the post-growth CVD process.

2. **Experimental Section**

CVD growth of MoS_2: We adapted a two-step synthesis of Te-doped MoS_2 monolayer alloys with varied compositions on the 300 nm SiO_2/Si substrates by CVD. The monolayer MoS_2 was synthesized first by the sulfurization of MoO_2. The MoO_2 powder (Sigma-Aldrich, 99%) and sulfur powder (Alfa Aesar, 99.5%) were used as the precursors. SiO_2/Si substrates were placed face-down to the MoO_2 powder (10 mg). The furnace was ramped to 750 °C in 35 minutes and then sulfur powder (80 mg) was

quickly heated to 110 °C. The whole system was held for 15 min for the growth. During the whole process 200 sccm Ar was used as the carrier gas.

Post-growth doping of Te via the second growth: Then the as-grown monolayer MoS_2 on the substrates was then transferred into another CVD system for the second-step growth and heated in a smaller one-end sealed quartz with different doping temperatures (T=600 ℃ , 650 ℃ , 700 °C). 1000 mg of tellurium powder (Alfa Aesar, 99.999%) were put in the upstream of the furnace with temperature around 550°C. The furnace was ramped to 600-700 °C in 20 min and held for 25 min for the tellurization. 50 sccm mixture gas of H_2/Ar (with 20% H_2) was used as the carrier gas.

The TEM samples were prepared by a traditional poly (methyl methacrylate) (PMMA) assisted method. PMMA solution (4% weight in anisole) was spin-coated on the wafer with Te-doped MoS2 monolayer alloys at 4000 rpm for 60 seconds and then baked at 120°C for 60 seconds. Afterwards, the wafer was floated on diluted HF solution (2%) to etch the SiO2 layer for 0.5-5 mins. Then the lift-off PMMA-MoS2(1-x)Te2x film was transferred to DI water for several times to wash away the residues. And a TEM grid (Quantifoil Mo grid) was used to pick up the film. The specimen was dried at 60 °C in ambient environment overnight, and then dropped into acetone for at least 8 hours to soak off the PMMA coating layer.

The structural characterizations were carried out with a probe corrected Titan ChemiSTEM (FEI Inc.). The microscope was operated at the acceleration voltage of 200 kV. The probe current was set at less than 80 pA and the convergence angle was about 22 mrad. And the collection angle is about 43.4 to 200 mrads. A GIF Quantum 965 X (Gatan Inc.) recorded electron energy loss spectra (EELS). XEDS data was recorded by a Bruker Super-X detector system.

All calculations are carried out with VASP and PBE exchange-correlation functional [34-36], adopting 500 eV plane-wave cutoff. For alloy calculations we used 5x5 supercells, where random substitution of Te atoms was modeled using the special quasirandom structures. The Brillouin zone was sampled with 2×2×1 k-point mesh. In ribbon calculations, the system size was 4 units along the ribbon and about 8 units normal to it (see Figure 8a for a side view). 2 k-points were used along the ribbon direction. Calculations demonstrating the Rashba effect were carried out with spin-orbit coupling, but otherwise in non-spin-polarized mode.

3. Result and Discussions

MoS_2 monolayers are grown on SiO_2/Si substrates via a CVD process, and then loaded into another CVD furnace for Te doping during which the as-grown MoS_2 samples were contained in a half-open mini-quartz tube to increase the partial pressure of Te, as shown in Figure 1a. The samples after tellurization on SiO_2/Si substrates are characterized by optical microscope (OM) as shown in Figure 1b, and that of pristine

MoS_2 monolayer is also given as a reference. For comparison, images of tellurized samples with and without H_2 carrier gas are displayed in the top and bottom panels, respectively. In the absence of H_2, we find that the as-grown MoS_2 monolayer starts to sublimate (like via oxidative etching) from the apex regions (arrows in the middle bottom panel) after the tellurization reaction proceeds for 10 minutes at 600 °C. As the tellurization time further increases, the flake is completely sublimated without any detectable residues (see bottom right panel). In contrast, in the presence of H_2 during tellurization, the products preserve their original morphology as found in the pristine monolayer MoS_2, as shown by the optical microscope images in the top panels. Figure 1c presents Raman spectra recorded on the MoS_2 after tellurization at 700 °C (green), 650 °C (pink), and 600 °C (orange) for 25 minutes, in which the spectra of pristine MoS_2 is also given as a reference (purple). The well-known characteristic resonance peaks of pristine 2H MoS_2 monolayer located at 383 cm^{-1} (known as E^1_{2g} mode) and 403 cm^{-1} (known as A_{1g} mode) are observed in all these samples, indicating the preservation of the 2H phase[37]. On the other hand, the appearance of a peak at 243 cm^{-1} at 600 °C, 650 °C, and 700 °C tellurization samples, corresponding to the E_{2g} mode of 2H-$MoTe_2$[27], not shown in 2H MoS_2 monolayer, provide evidence that the Te atoms were successfully substituted. In order to synthesize Te-doped MoS_2 monolayer alloys, hydrogen as a strong reducer is required due to the low chemical reactivity of Te, which is similar to the synthesis of Se-based TMDC materials (like $MoSe_2$, WSe_2) [38, 39]. And during this substitution reaction, S vacancy [40] could be produced by the introduction of hydrogen at high temperature, which can promote the substitution

reaction of the S with Te atoms. We propose that the chemical reaction during the tellurization of MoS_2 is as follows:

$$MoS_2 + 2H_2 + 2Te \rightarrow MoTe_2 + 2H_2S$$

We then turn to the electron microscopy characterization of the microscopic structure and chemical composition of the tellurized MoS_2 samples. Figure 2a shows a low-magnification ADF-STEM image of a Te-doped MoS_2 (700 °C, 25 min) flake with well-preserved triangular shape. Chemical analysis via electron energy loss spectroscopy (EELS) and X-ray energy-dispersive spectrometer (XEDS) over 50 samples both confirm the existence of Te atoms, with typical spectra displayed in Figure 2b (EELS) and Figure 2c (XEDS). Note that here both the EELS and XEDS spectra were collected over a large number of samples and reflect the average chemical composition, not locally. The appearance of oxygen K-edge at 532 eV in the EELS spectra may come from the residual PMMA that were used during the sample transfer.

To analyze in more detail the statistical distribution of the Te substitution sites, we carried out atomically resolved ADF-STEM characterization over large number of samples and sample areas. Shown in Figure 3a-c are three representative ADF-STEM images of the Te-doped MoS_2 monolayers prepared under different tellurization conditions, corresponding to 600 °C, 650 °C, and 700 °C for 25 minutes. These ADF-STEM images are Z-contrast images [41], which enables straightforward identification of the Te substitution sites (marked with yellow circles), although the top and bottom chalcogen sublattices cannot be separated. Fig 4a, b (650°C for 25 minutes) show the

result where the different types of sites are indicated (yellow circle represent S2 site, green and blue, respectively S + Te site and Te2 site). Next, we analyze the alloying degree (J) for Te (include Te2 site and S + Te site). The value of alloying degree (J) can be given as

$$J_{Te} = P_{observed} / P_{random} \times 100\% \quad [9] \qquad (1)$$

Where $P_{observed}$ is the ratio of the averaged S coordination number to the total coordination number and P_{random} is the atomic ratio of S in the examined layer. J_{Te} close to 100% means that the Te and S atoms are distributed randomly around the Te sites. J_{Te}<100% means a homophilic configuration, while J_{Te}>100% implies a heteroatom-rich configuration. J_{S2} can also be obtained from the same ADF image. As shown in Figure 4c, the average of J_{Te} is 100.6% and J_{S2} is 98.4%, indicating that the Te distribution is very close to random substitution. Note: A recent study by Fang et al. [42] reported a phase separation in the $MoS_{2(1-x)}Te_{2x}$ which may be caused due to the lower tellurization temperature (500 °C) used there.

Figure 4d shows the relationship between the growth temperature and the corresponding substituted Te atom proportion. After statistical analysis of dozens of atomically resolved STEM images in different growth temperatures, it was found that the Te ratio N_{Te} / (N_{Te} + N_S), where the N_{Te} is the number of Te atoms, and N_S is the number of S atoms increases steadily with the growth temperature, yielding 3.3%, 6.6%, and 27.3% for samples grown at 600 °C, 650 °C, and 700 °C, respectively, for 25 min. The post-growth process adopted here, with MoS_2 sheet placed on substrate and only

the top side exposed to the tellurization, could naturally lead to Te asymmetry in the two sides of the sheet. From the STEM images, we cannot distinguish which S atom was replaced by Te atom. Based on an assumption of random substitution, we evaluated statistical estimates of the site proportions (see SI) and compared them to the experimental proportions in Figure 4d, which indicated that the samples could show at least partial Te asymmetry.

Having assessed the composition and possible composition asymmetry, we analyze the stability of these structures with the help of density functional theory calculations. We generated models with randomly substituted Te, both in the symmetric and asymmetric configurations. We define the mixing enthalpy (at 0 K)

$$E_{mix} = E_{MoS_{2x}Te_{2(1-x)}} - [x * E_{MoS_2} + (1-x) * E_{MoTe_2}] \qquad (2)$$

where the energies on the right side refer to DFT total energies. Mixing free energy is then obtained by adding the entropy of mixing and here evaluated at 650 C. The results in Figure 5 show that there are no limits for mixing ($E_{mix}<0$) when Te is substituted symmetrically on both sides and without strain. When Te is substituted on only the top sublattice, we obtain a limit of 33 % (or 66% of the top sublattice sites), above which segregation is expected. Since the lattice constant could be close to that of MoS_2 during the tellurization, we repeated the calculations with the lattice constant fixed to that of MoS_2. The obtained limits for mixing in the symmetric and asymmetric case are 28 % and 19 %, respectively. The limits in the unstrained asymmetric and strained symmetric cases both agree well with the experiment, suggesting that the composition is limited

either by the strain or by the asymmetry, but it is difficult to draw conclusions on the amount of asymmetry from these results.

In the relatively gentle growth conditions (600 °C, 650 °C), the structure retains the hexagonal lattice and shows no significant difference from the MoS_xSe_y alloys [6]. On the other hand, as Te proportion increases (sample grown at 700 °C, corresponding to Te ratio of 27.3%), it seems that the Te atoms tend to aggregate (Figure 6a), which is different from the MoS_xSe_y alloy case. We notice local structural modulations, where the aggregated Te atoms tend to form triangular regions, as outlined by purple triangle in Figure 6a. In few cases, the Te atoms are located in between the neighboring Mo atoms, forming an atomic chain, as highlighted by yellow lines. Figure 6b, c show the distortion structure in Te-doped MoS_2 monolayer alloys grown at 700 ℃ . Triangles with excess or deficiency of Te are shown in Figure 6b, c and marked in purple. The triangles are surrounded by the chain-like structures that could originate from displacement of Te atoms due to buildup of strain during the growth. The schematic of outward displacement of Te atoms is shown in Figure 6b, in which purple arrows (and orange ones in ADF-image) illustrate the shift direction of Te atoms. The gathered Te atoms shift away from the origin X_2 sites radially, leading to a triangle in which center Te atom still located in the X_2 site. At the edge of such distortion triangles, the Te atoms are located right between two nearby Mo atoms, with Mo-Te-Mo angle (projected angle) at 180°, forming atomic chains. Around the Te-deficient regions, shown as a triangle with dimmer contrast in Figure 6c, the Te atoms move towards the undoped regions.

Considering the atomic chains in more detail, Figure 6d, e show the X_2 sites across the triangle and along the atom chain. It is found that the intensity at X_2 sites along the atomic chain are relatively lower than in the undistorted parts, indicating the disappearance of S atoms, with the possible structure shown in Figure 6d, e. The S vacancies could be generated to release the strain induced by the Te substitution. Linear arrangements are known to be the lowest energy configuration for vacancies in MoS_2 [43, 44]. Here, the vacancies appear to similarly agglomerate to lines, finally leading to the observed local reconstruction of the alloy structure. As previously reported for MoS_2 and $MoSe_2$ [44-47], electron beam irradiation creates S vacancies in the lattice, and provides the energy for the vacancies to overcome the migration energy barrier. In our observation, high growth temperature instead of electron beam likely offers the energy for migration, and could also explain the increased vacancy concentration. In addition, the vacancies could be created by the strain buildup. The calculated vacancy formation energies as a function of alloy concentrations are shown in Figure 5b. In the case of unstrained lattice, the formation energies are close to those in pristine MoS_2, but under strain the formation energy decreases strongly, which would then give rise to increased vacancy concentration. Overall, the case of Te substitution appears to differ markedly from that with Se. The Se concentration can be continuously tuned in the $MoS_{2(1-x)}Se_{2x}$ monolayer alloys without disturbing the 2H phase lattice, while there appears to be intrinsic limits in the case of Te. Moreover, when close to this limit, the local structure becomes distorted due to either the 10% lattice mismatch (3.161 Å and 3.518 Å for MoS_2 and MoTe2, respectively) or the 16.7% difference in the ionic radii

of (R_S=1.84 Å and R_{Te}=2.21 Å for S^{2-} and Te^{2-}). This is consistent with the experimental results as shown in Fig. S6 where the lattice constant of the doped MoS_2 monolayer becomes larger as the Te concentration increases.

Finally, we discuss the electronic structure and optical properties of our samples. The photoluminescence spectra of the samples are shown in Figure 7a. The peak position, assigned to A exciton, shifts to lower energies and the intensity decreases rapidly as the Te concentration increases. The peak positions as a function of the composition are collected in Figure 7b, where we compare them to the calculated band gap values (shifted to match the MoS_2 value at the endpoint). The agreement is clearly better with respect to the calculations with unstrained lattice, whereas the degree of asymmetry does not seem to play a large role. In addition, we plotted effective band structures of all the alloy configurations (Figure S2), which indicate that the band gap changes from direct (K-K) to indirect (Γ-K) at around 10% Te in the asymmetric and unstrained case. In the symmetric case, the gaps remains direct for the unstrained systems, but again changes to indirect (K-T) at around 10% Te. It is worth noting, that the band structures are only weakly distorted in comparison to the pristine ones, i.e., they do not show pronounced defect states localized on the Te atoms, and thus it seems unlikely that the intensity change could be assigned to strong increase in non-radiative recombination rate.

Taken alone, the calculated mixing limits, the vacancy concentration, and the PL intensity variation could all be assigned to either symmetric (and strained) or asymmetric (and unstrained) configurations, whereas the statistical analysis gives weak indication that Te is preferentially substituted in the top of the sheet. On the other hand, PL peak positions strongly points to unstrained samples, which, when coupled with the mixing limits, suggest asymmetric distribution (there should be no concentration limits in the unstrained symmetric case, in contradiction with the experiments). Thus, we tentatively assign our samples to be the asymmetric-type Janus structures[48] of $MoS_{2(1-x)}Te_{2x}$. Asymmetric Te distribution is expected to induce bending strain in the sheet. The radius of curvature is evaluated using a ribbon geometry as shown on top of Figure 8a, and seen to be fairly small at larger Te concentrations. The associated energy cost for keeping the layer flat instead of bending can be quantified from the energy difference between the symmetric and asymmetric systems and scaled to the area of the sheet, and is shown in Figure 8b. The bending energy is found to be relatively small at less than 16 meV/Å^2. This can be compared to the binding energy of MoS_2 sheet to SiO_2, which was calculated to be about 13-15 meV/Å^2 in Ref. [49] or to typical binding energies in layered systems of about 20 meV/Å^2 [50]. We conclude that the interaction with the substrate is sufficiently strong to prevent the system from bending for all but the highest concentrations (or concentration imbalance).

The asymmetry can also lead to interesting properties since it breaks the mirror symmetry and essentially leads to internal electric field perpendicular to the sheet. This

for instance generates Rashba splitting of the VBM states at the Γ-point [51, 52]. The effective band structure for the case of 32% asymmetric Te concentration is shown in Figure 7c. The inset shows zoom-in to the VBM around Γ-point, where the states are colored by the spin-component perpendicular to the k-point and in-plane. The (normally spin-degenerate) VBM states exhibit Rashba-type splitting, that is linear in k and with the spin orientation perpendicular to k. At the VBM, located in k=0.02 2π/a, the splitting is about 10 meV.

4. Conclusion

In summary, we have shown that $MoS_{2(1-x)}Te_{2x}$ monolayers can be synthesized by the tellurization of MoS_2 via tuning CVD parameters. The type and distribution of Te atoms have been analyzed based on ADF images. A large area of local distortion and single atom chain was observed at a higher deposition temperature. Due to the introducing of metallic Te element, $MoS_{2(1-x)}Te_{2x}$ alloys can have larger-range tunable band-gap (~0.7eV) than $MoS_{2(1-x)}Se_{2x}$ alloys (~0.3eV) [53], which broadens its application in nanoelectronics and nanophotonics. Comparison of experimental results and first principles calculations led us to conclude that the Te substitution preferentially takes place in the top chalcogen sublattice. The asymmetric distribution leads to unusual physical properties, such as the change from direct to indirect gap and Rashba-type splitting of the VBM. Recently, it has also been reported that the superconductivity in $MoTe_2$ single crystal can be greatly enhanced by the partial S substitution [29]. This

work gives insight for CVD growth of Te-doped 2D TMD alloys with controlled composition and could empower the further study on its electronics and optoelectronics.

Acknowledgements

This work was financially supported by the National Science Foundation of China under Grants 51772265, 61721005, 61571197, 61172011 and 5122202, the National Basic Research Program of China under Grants 2014CB932500 and 2015CB 921004 and the 111 project under Grant B16042. H.P.K., A.H., and A.V.K. acknowledge the Academy of Finland for the support under Project No.~286279 and through its Centres of Excellence Programme (2012-2017) under Project No.~251748. H.P.K. and A.V.K. also acknowledge support from the U.S. Army RDECOM via contract No. W911NF-15-1-0606.

The work on electron microscopy was done at the Center of Electron Microscopy of Zhejiang University. We also thank Prof. Jianguang Zhou for the generous grants of PL and Raman machine time.

References

[1] Radisavljevic B, Radenovic A, Brivio J, Giacometti V and Kis, A 2011 Single-layer MoS_2 transistors *Nat. Nanotechnol. 6* 147-150

[2] Mak K F, He K, Shan J and Heinz T F 2012 Control of valley polarization in monolayer MoS_2 by optical helicity *Nat. Nanotechnol. 7* 494-498

[3] Wang Q H, Kalantar-Zadeh K, Kis A, Coleman J N and Strano, M. S. 2012 Electronics and optoelectronics of two-dimensional transition metal

dichalcogenides *Nat. Nanotechnol. 7* 699-712

[4] Radisavljevic B and Kis A. 2013 Mobility engineering and a metal-insulator transition in monolayer MoS_2 *Nat. Mater. 12* 815-820

[5] Yin X, Ye Z, Chenet D A, Ye Y, O'Brien K Hone, J C and Zhang, X. 2014 Edge nonlinear optics on a MoS_2 atomic monolayer *Science 344* 488-490.

[6] Gong Y et al 2013 Band gap engineering and layer-by-layer mapping of selenium-doped molybdenum disulfide *Nano Lett. 14* 442-9

[7] Duan X et al 2016 Synthesis of $WS_{2x}Se_{2-2x}$ alloy nanosheets with composition-tunable electronic properties *Nano Lett. 16* 264-269

[8] Li X et al 2016 Isoelectronic tungsten doping in monolayer $MoSe_2$ for carrier type modulation. *Adv. Mater.*

[9] Dumcenco D O, Kobayashi H, Liu Z, Huang Y S and Suenaga K 2013 Visualization and quantification of transition metal atomic mixing in $Mo_{1-x}W_xS_2$ single layers *Nat. Commun. 4*, 1351.

[10] Chen, Y, Xi, J, Dumcenco, D. O, Liu, Z, Suenaga, K, Wang, D, Shuai, Z, Huang, Y. S, Xie, L. 2013 Tunable band gap photoluminescence from atomically thin transition-metal dichalcogenide alloys. *ACS Nano 7* 4610-4616

[11] Zhang M et al 2014 Two-dimensional molybdenum tungsten diselenide alloys: photoluminescence, Raman scattering, and electrical transport *ACS Nano 8* 7130-7137

[12] Feng Q et al 2014 Growth of large-area 2D $MoS_{2(1-x)}Se_{2x}$ semiconductor alloys *Adv. Mater. 26* 2648-2653

[13] Feng Q, Mao N, Wu J, Xu H, Wang C, Zhang J and Xie L. 2015 Growth of $MoS_{2(1-x)}$ Se_{2x} (x= 0.41–1.00) Monolayer alloys with controlled morphology by physical

vapor deposition *ACS Nano 9 7450-7455*

[14] Mann J et al 2014 Two-Dimensional transition metal dichalcogenides with tunable direct band gaps: $MoS_{2(1-x)}Se_{2x}$ monolayers *Adv. Mater. 26* 1399-1404

[15] Su S H, Hsu Y T, Chang Y H, Chiu M H, Hsu C L, Hsu W T, Chang W H, He J H and Li L J 2014 Band gap-tunable molybdenum sulfide selenide monolayer alloy *Small 10* 2589-2594

[16] Ruppert C, Aslan O B and Heinz T F. *2014* Optical properties and band gap of single-and few-layer $MoTe_2$ crystals *Nano Lett. 14 6231-6236*

[17] Cho, S et al 2015 Phase patterning for ohmic homojunction contact in $MoTe_2$ *Science 349* 625-628

[18] Keum D H et al 2015 Bandgap opening in few-layered monoclinic $MoTe_2$ *Nat. Phys. 11* 482-486

[19] Qi Y et al 2016 Superconductivity in Weyl Semimetal Candidate $MoTe_2$ *Nat. Commun. 7* 11039

[20] Naylor C H et al 2016 Monolayer single-crystal 1T'-$MoTe_2$ grown by chemical vapor deposition exhibits weak antilocalization effect *Nano Lett. 16* 4297-4304

[21] Ali M N et al 2014 Non-saturating magnetoresistance in WTe_2 *Nature 514* 205-208

[22] Pan X C et al 2015 Pressure-driven dome-shaped superconductivity and electronic structural evolution in tungsten ditelluride *Nat. Commun. 6* 7805

[23] Wang L, Gutierrez Lezama I, Barreteau C, Ubrig N, Giannini E, and Morpurgo, A F 2015 Tuning magnetotransport in a compensated semimetal at the atomic scale *Nat. Commun. 6* 8892

[24] Qian X, Liu J, Fu L and Li J 2014 Quantum spin hall effect in two-dimensional

transition metal dichalcogenides *Science 346* 1344-1347

[25] Pletikosic I, Ali M N, Fedorov A V, Cava R J and Valla T 2014 Electronic structure basis for the extraordinary magnetoresistance in WTe_2 *Phys. Rev. Lett. 113* 216601

[26] Soluyanov A A, Gresch D, Wang Z, Wu Q, Troyer M, Dai X and Bernevig B A 2015 Type-II Weyl semimetals *Nature 527* 495-498

[27] Yamamoto M, Wang S T, Ni M, Lin Y F, Li S L, Aikawa S, Jian W B, Ueno K, Wakabayashi K and Tsukagoshi K 2014 Strong enhancement of Raman scattering from a bulk-inactive vibrational mode in few-layer $MoTe_2$ *ACS Nano 8* 3895-3903

[28] Sun Y et al 2016 Low-temperature solution synthesis of few-layer 1T'-$MoTe_2$ nanostructures exhibiting lattice compression *Angew. Chem. Int. Ed. 55* 2830-2834

[29] Chen F C et al 2016 Superconductivity enhancement in the s-doped Weyl semimetal candidate $MoTe_2$ *Appl. Phys. Lett. 108* 162601

[30] Sun Y, Wu S C, Ali M N, Felser C and Yan B 2015 Prediction of Weyl semimetal in orthorhombic $MoTe_2$ *Phys. Rev. B 92* 161107

[31] Deng K et al 2016 Experimental observation of topological fermi arcs in type-II Weyl semimetal $MoTe_2$. *Nat. Phys.*

[32] Jiang J et al 2017 Signature of type-II Weyl semimetal phase in MoTe2 *Nat. Commun*. 8 13973

[33] Xu N et al 2016 Discovery of Weyl semimetal state violating Lorentz invariance in $MoTe_2$ arXiv:1604.02116. arXiv.org e-Print archive. https://arxiv.org/ftp/arxiv/papers/1604/1604.02116.pdf (accessed).

[34] Kresse G and Joubert D. 1999 From Ultrasoft Pseudopotentials to the Projector Augmented-Wave Method *Phys. Rev. B* 59 1758

[35] Kresse G and Furthmüller J 1996 Efficient Iterative Schemes for ab Initio Total-

Energy Calculations Using a Plane-Wave Basis Set *Phys. Rev. B* 54 11169

[36] Perdew J P Burke K and Ernzerhof M 1996 Generalized Gradient Approximation Made Simple *Phys. Rev. lett.* 77 3865

[37] Li H, Zhang Q, Yap C C R, Tay B K, Edwin T H T, Olivier A and Baillargeat, D 2012 From bulk to monolayer MoS_2: Evolution of raman scattering *Adv. Func. Mater. 22* 1385-1390

[38] Huang J K, Pu J, Hsu C L, Chiu M H, Juang Z Y, Chang Y H, Chang W H, Iwasa Y, Takenobu T and Li L J 2014 Large-area synthesis of highly crystalline WSe_2 monolayers and device applications *ACS Nano 8* 923-930

[39] Wang X et al 2014 Chemical vapor deposition growth of crystalline monolayer $MoSe_2$ *ACS Nano 8* 5125-5131

[40] Kim B H et al 2013 Effect of sulphur vacancy on geometric and electronic structure of MoS_2 induced by molecular hydrogen treatment at room temperature. *RSC Advances* 3 18424-18429

[41] Krivanek O L et al 2010 Atom-by-atom structural and chemical analysis by annular dark-field electron microscopy *Nature 464* 571-574

[42] Fang Q et al 2017 Transformation of monolayer MoS_2 into multiphasic $MoTe_2$: chalcogen atom-exchange synthesis route Nano Res. 10 2761–2771

[43] Komsa H P, Kurasch S, Lehtinen O, Kaiser U and Krasheninnikov A V 2013 From point to extended defects in two-dimensional MoS_2: evolution of atomic structure under electron irradiation *Phys. Rev. B 88* 035301

[44] Komsa H P, Krasheninnikov A V 2017 Engineering the Electronic Properties of Two-Dimensional Transition Metal Dichalcogenides by Introducing Mirror Twin Boundaries *Adv. Electron. Mater.* 3 1600468

[45] Lehtinen O et al 2015 Atomic scale microstructure and properties of Se-deficient two-dimensional $MoSe_2$ *ACS Nano 9* 3274-3283

[46] Lin, J Pantelides, S T and Zhou W 2015 Vacancy-induced formation and growth of inversion domains in transition-metal dichalcogenide monolayer *ACS Nano 9* 5189-5197

[47] Wang S, Lee G D, Lee S, Yoon E and Warner J H 2016 Detailed atomic reconstruction of extended line defects in monolayer MoS_2 *ACS Nano 10* 5419-5430

[48] Lu A Y et al 2017 Janus monolayers of transition metal dichalcogenides *Nat. Nanotechnol.*

[49] Dolui K, Rungger I and Sanvito S 2013 Origin of the n-Type and p-Type Conductivity of MoS2 Monolayers on a SiO 2 Substrate *Phys. Rev. B* 87 165402

[50] Björkman T, Gulans A, Krasheninnikov A V and Nieminen R M. 2012 Van der Waals Bonding in Layered Compounds from Advanced Density-Functional First-Principles Calculations *Phys. Rev. Lett.* 108 235502

[51] Zhu Z Y, Cheng Y C and Schwingenschlögl U 2011 Giant spin-orbit-induced spin splitting in two-dimensional transition-metal dichalcogenide semiconductors. *Phys. Rev. B* 84 153402

[52] Yao Q F et al 2017 Manipulation of the large Rashba spin splitting in polar two-dimensional transition-metal dichalcogenides *Phys. Rev. B* 95 165401

[53] Komsa H P and Krasheninnikov A V 2012 Two-dimensional transition metal dichalcogenide alloys: stability and electronic properties *J. Phys. Chem. Lett*. 3 3652-3656

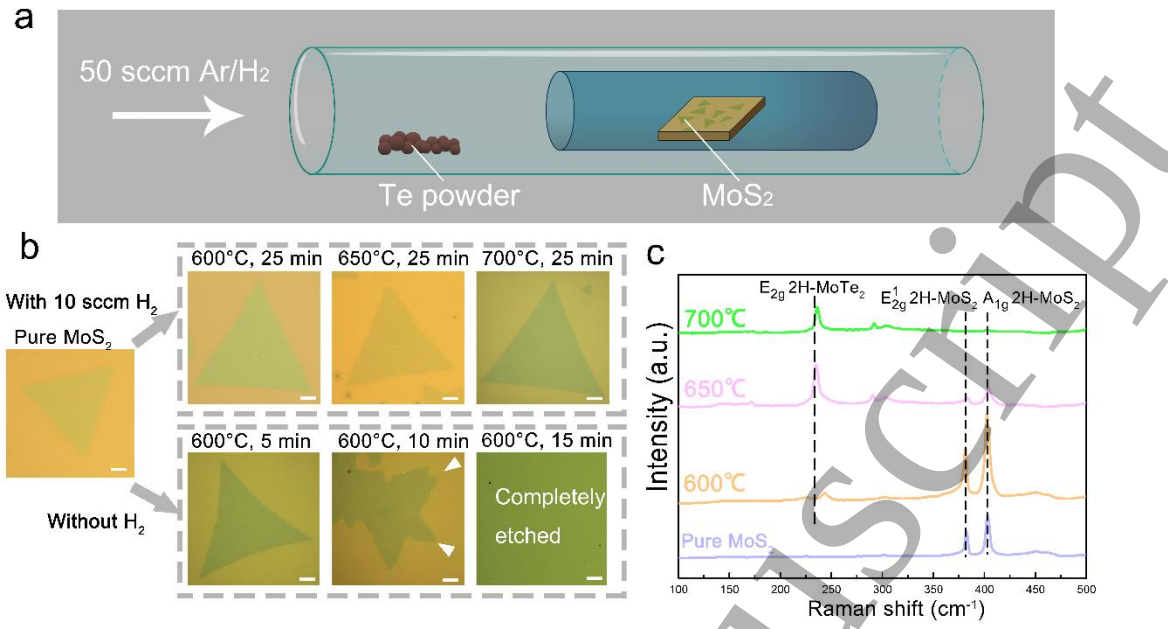

Figure 1. (a) Schematic setup for the post-growth doping. (b) Typical optical images of monolayer MoS_2 before (left) and after doping with tellurium under different conditions: with 10 sccm H_2 (top right row), without H_2 (right bottom row). Detailed conditions (temperature and reaction time) are listed above each display. Scale bar = 5 μm in all displays. (c) Raman spectra of Te-doped MoS_2 monolayer alloys grown at same doping time (25 min) and different doping temperature.

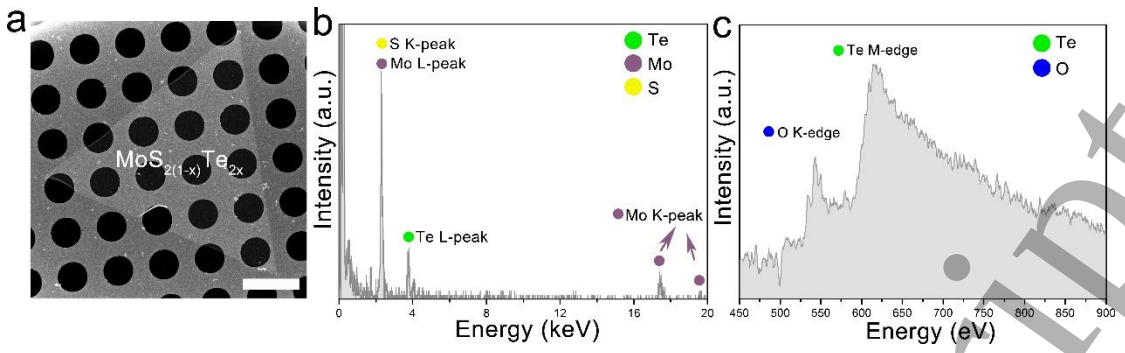

Figure 2. (a) Low-magnification ADF-STEM image of single crystal Te-doped MoS_2 monolayer alloys. Scale bar: 5 μm. (b) EELS spectra substantiates the existence of Te element. (c) XEDS spectra again confirms the presence of Te element. The EELS curve was smoothed by the origin software for a better display.

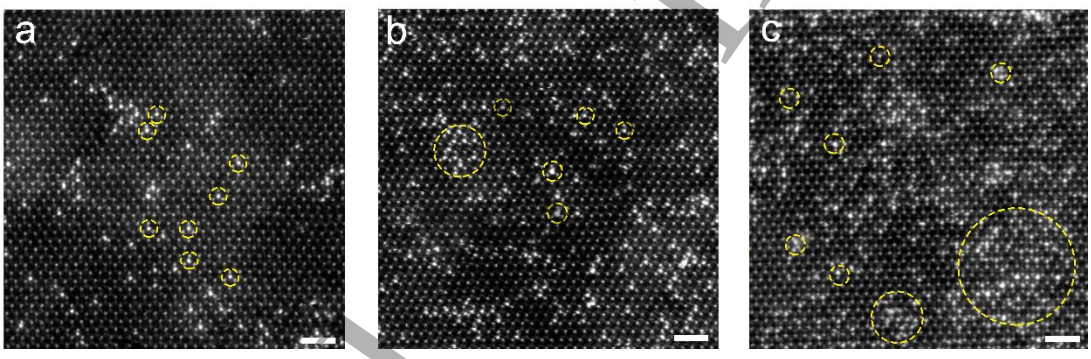

Figure 3. (a-c) Atomically resolved ADF-STEM images and b-axis atomic structure of Te-doped MoS_2 monolayers at different growth temperature. A number of bright sites corresponding to the local Te sites can be distinguished from the Z-contrast images (mark with yellow circles). (a) 600 °C, 25 min; (b) 650 °C, 25 min; (c) 700 °C, 25 min. Scale bar: 1 nm.

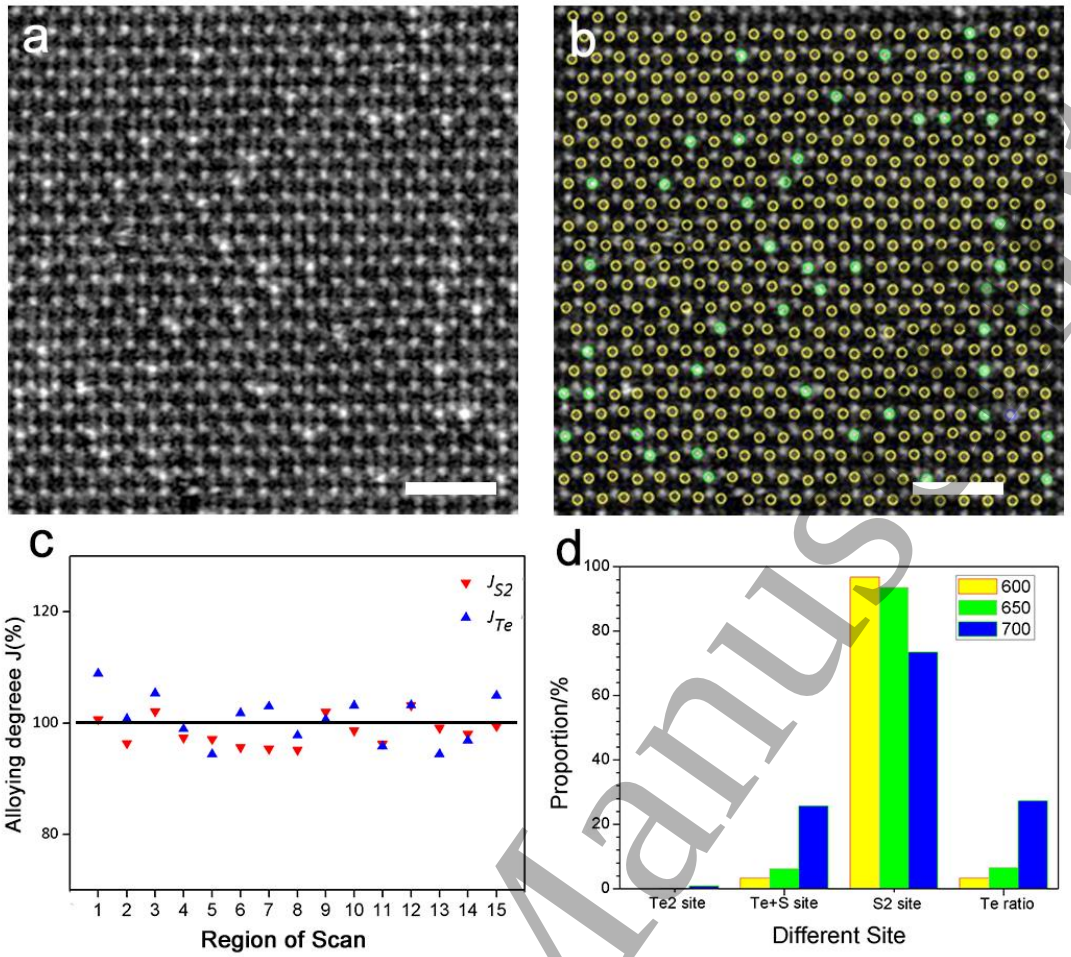

Figure 4. (a) Atomic-resolved ADF- STEM image of $MoS_{2(1-x)}Te_{2x}$ monolayer, and (b) the distribution of chalcogen atoms in $MoS_{2(1-x)}Te_{2x}$ monolayer(yellow circle represent S2 site, green and blue, respectively S + Te site and Te2 site). The Te substitution was conducted at 650 °C. Scale bar: 1 nm (c) The analyzed alloying degree in $MoS_{2(1-x)}Te_{2x}$ monolayers from different samples which were tellurized at different temperatures (600, 650 and 700).. (d) Summary of the growth conditions and Te proportion for all synthesized Te doped monolayer alloys.

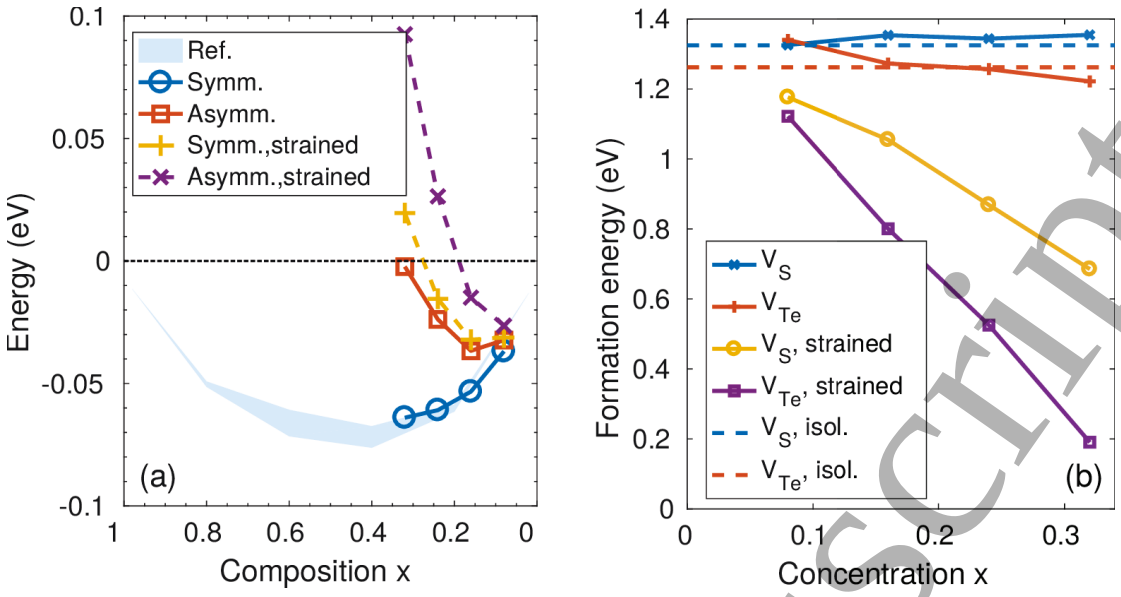

Figure 5. (a) Mixing free energy (at 650 C) as a function of the alloy concentration x, with Te substituted either symmetrically in both top and bottom sublattices or asymmetrically only in the top sublattice. Also shown are the results from strained lattice, with lattice constant fixed to that of MoS_2. The computational reference data is from Ref. 48. (b) Vacancy formation energies as a function of alloy concentrations. Both unstrained lattice and that strained to MoS_2 lattice constant are considered.

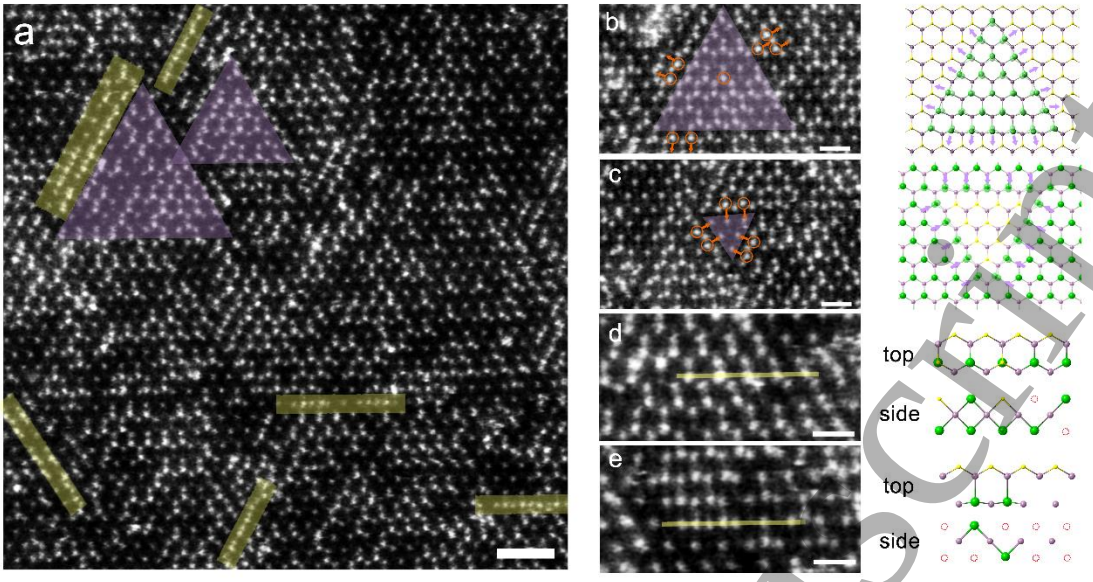

Figure 6. (a) Atomic resolved STEM-ADF images of Te-doped MoS2 monolayer alloys grown at 700 °C for 25 min. The purple triangle indicate the local structure modulation. Te atom stands in the middle of two Mo atoms, forming an atomic chain, which was highlighted by yellow lines. Scale bar: 1 nm. (b, c) STEM-ADF images and schematic of local structure distortion. Purple: Mo; yellow: S; green: Te. Orange arrows illustrated the shift direction of Te atoms. (d, e) STEM-ADF images and schematic of possible structure of atomic chain. Scale bar: 0.5 nm

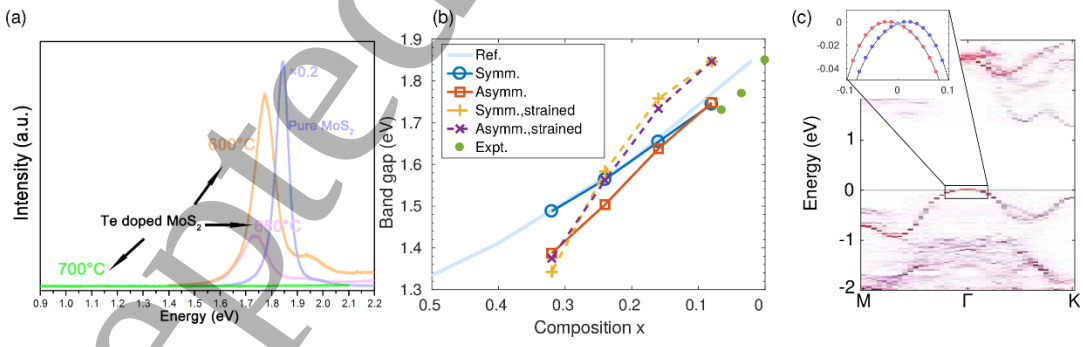

Figure 7. (a) Measured photoluminescence spectra from the three samples grown at different temperatures and compared to pristine MoS_2. (b) Comparison of experimental band gaps to the calculated band gap variations with different Te distributions and with or without strain. (c) Effective band structure of the asymmetric unstrained system with

32% Te. The states are colored by their projection to S atoms (red) and Te atoms (blue). Inset: Zoom-in to the valence band maximum around Γ-point showing Rashba effect. Here the states are colored according to the spin-projection in y-direction, when k-points are in x-direction.

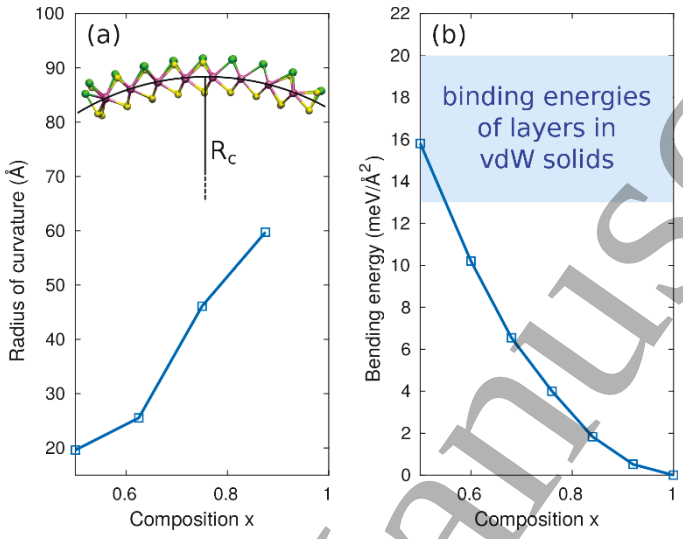

Figure 8. (a) Radius of curvature induced to the system by the asymmetric Te distribution as a function of composition. (b) Bending energy per area of sheet compared to typical vdW binding energies. Red line: energy cost estimated from the ribbon calculations.